Cryogenic electron microscopy structures reveal how ATP and DNA binding in MutS coordinates sequential steps of DNA mismatch repair

Borsellini, A.; Kunetsky, V.; Friedhoff, P.; Lamers, M.H.

nature structural & molecular biology

ARTICLES

https://doi.org/10.1038/s41594-021-00707-1

Cryogenic electron microscopy structures reveal how ATP and DNA binding in MutS coordinates sequential steps of DNA mismatch repair

Alessandro Borsellini[1], Vladislav Kunetsky[2], Peter Friedhoff[2] and Meindert H. Lamers[1]✉

DNA mismatch repair detects and corrects mismatches introduced during DNA replication. The protein MutS scans for mismatches and coordinates the repair cascade. During this process, MutS undergoes multiple conformational changes in response to ATP binding, hydrolysis and release, but how ATP induces the various MutS conformations is incompletely understood. Here we present four cryogenic electron microscopy structures of *Escherichia coli* MutS at sequential stages of the ATP hydrolysis cycle that reveal how ATP binding and hydrolysis induce closing and opening of the MutS dimer, respectively. Biophysical analysis demonstrates how DNA binding modulates the ATPase cycle by prevention of hydrolysis during scanning and mismatch binding, while preventing ADP release in the sliding clamp state. Nucleotide release is achieved when MutS encounters single-stranded DNA that is produced during removal of the daughter strand. The combination of ATP binding and hydrolysis and its modulation by DNA enables MutS to adopt the different conformations needed to coordinate the sequential steps of the mismatch repair cascade.

DNA mismatch repair (MMR) is an evolutionary conserved mechanism that removes mispaired bases from DNA after DNA replication. In doing so, it reduces the mutation frequency 100–1,000-fold, preventing cancer and drug resistance. MMR also plays roles in regulation of recombination, triplet repeat expansion and DNA damage signaling[1,2]. The repair process consists of a cascade of proteins that act sequentially. The protein MutS scans DNA for mismatches and, upon detection, recruits a second protein, MutL. In *Escherichia coli*, MutL subsequently activates the endonuclease MutH that creates a nick in the newly synthesized strand at hemimethylated GATC sites[3–5]. In other species, including eukaryotes, endonuclease activity resides in the MutL homologs themselves[6,7] and is directed to the newly synthesized strand by the DNA sliding clamp (β or PCNA)[8,9]. In bacteria, the single-stranded nick then creates an entry point for the UvrD helicase (RecD2 in some *Bacillus* species)[10,11] that, with the aid of a 5′–3′ or 3′–5′ exonuclease, excises the newly synthesized strand[12,13]. The stretch of DNA thus removed is then resynthesized by a DNA polymerase and the remaining nick sealed by a DNA ligase[14]. In eukaryotes the strand removal process is less well understood, but involves the replicative DNA polymerase δ and exonuclease EXO1 (refs. [14,15]).

Throughout this process, MutS is the master coordinator that initiates the subsequent steps of the repair cascade. First, it scans the genome in search for a mismatch. Once bound to a mismatch, it undergoes a conformational change into a sliding clamp that recruits MutL[16,17]. In the clamp state, MutS remains on DNA for prolonged times and releases it only when it encounters a DNA end[18,19] or a single-stranded DNA gap[20,21]. In this way, MutS molecules remain present on DNA until the mismatch has been removed and the repair process is terminated. We recently reported cryogenic electron microscopy (cryo-EM) structures of MutS on DNA at different stages of the repair process, revealing the multiple conformations that enable it to perform its different tasks[22]. ATP binding and hydrolysis are essential for switching of MutS between different states[23], but the molecular basis of these transitions and how they are regulated remain unresolved.

To gain insight into ATP-induced conformational changes of MutS, we have now determined four structures of apo MutS at sequential stages of the ATP hydrolysis cycle: (1) ADP-bound, (2) ATP-bound, (3) bound to the nonhydrolyzable ATP analog AMPPNP and (4) bound to the transition-state analog ADP-vanadate[24] (ADP-VO_4^{3-}/ADP-Vi). Our structures show how an open MutS dimer in the ADP-bound form closes upon binding to a single ATP but does not reach a hydrolysis-competent active site. Only upon binding of two triphosphate nucleotides is a complete active site formed that can hydrolyze ATP. Supporting biochemical analysis reveals how ATP and DNA binding work together to initiate the subsequent steps of the repair cascade. During both DNA scanning and mismatch binding, DNA keeps the ATPase domains in an open, noncatalytic state in which nucleotide binding sites are free to exchange ADP for ATP. Two ATP molecules are needed to transform MutS into the sliding clamp conformation that recruits MutL. In this clamp state, ATPase active sites are completed and can hydrolyze ATP. However, the double-stranded DNA substrate keeps the nucleotide binding sites closed and prevents nucleotide release until MutS reaches a stretch of ssDNA where interactions with the dsDNA are lost. This enables the dimer to open up and reset the ATPase site for a new round of ATP and DNA binding.

Results

Cryo-EM structures of MutS during the ATP hydrolysis cycle. To gain insight into the mechanism of ATP hydrolysis in MutS, we determined cryo-EM structures of the MutS dimer in the absence of DNA at sequential stages of the hydrolysis cycle: (1) bound to two ADP molecules, (2) bound to one ADP and one ATP, (3) bound to two AMPPNP molecules and a nonhydrolyzable ATP analog and (4) bound to two ADP-Vi molecules, a transition-state analog, to

[1]Department of Cell and Chemical Biology, Leiden University Medical Center, Leiden, the Netherlands. [2]Institute for Biochemistry, Justus-Liebig University, Giessen, Germany. ✉e-mail: m.h.lamers@lumc.nl

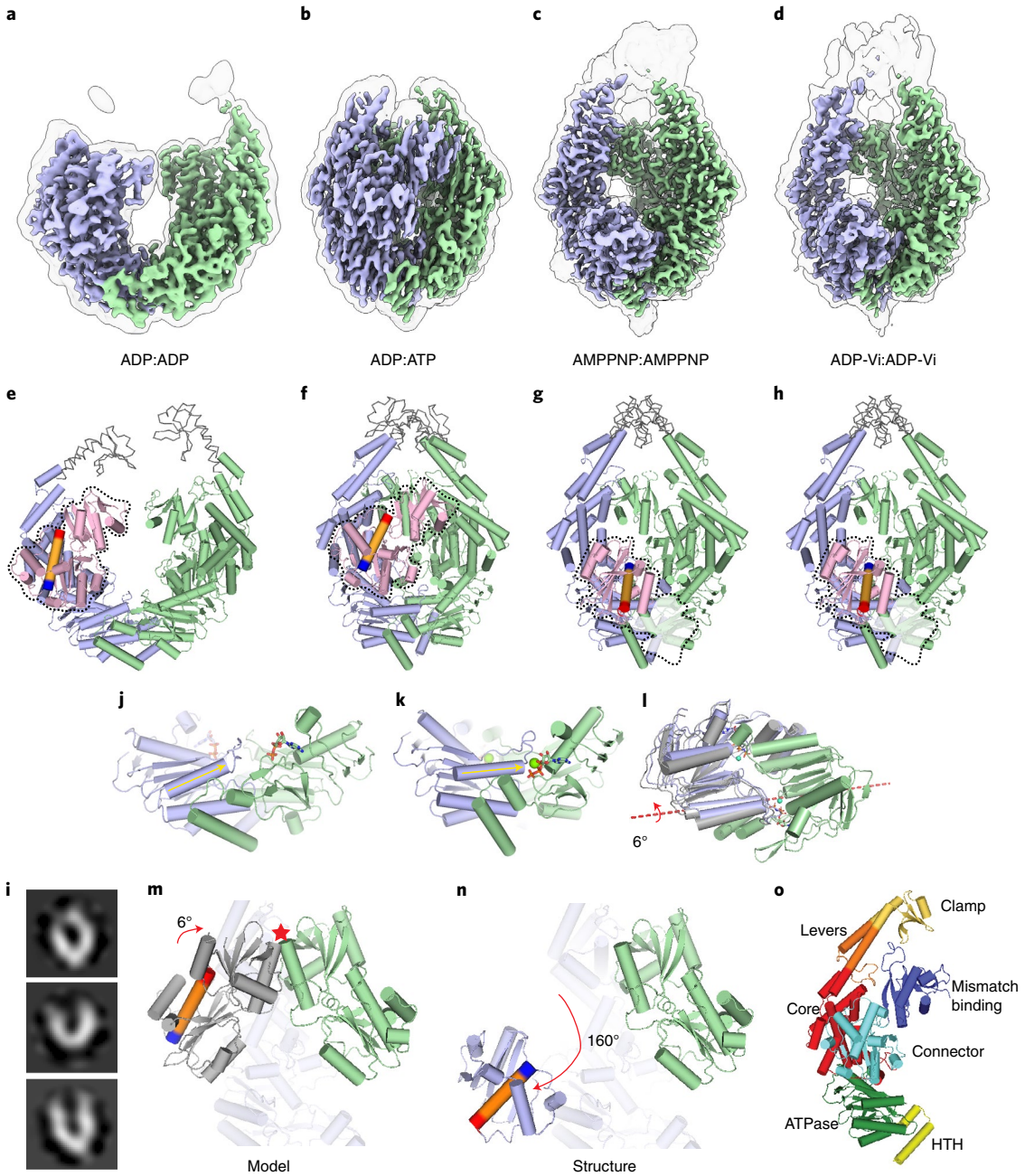

Fig. 1 | Structures of MutS at sequential steps of the ATP hydrolysis cycle. a–**d**, Cryo-EM maps of ADP- (**a**), ATP- (**b**), AMPPNP- (**c**) and ADP-Vi-bound MutS (**d**). Monomer A is shown in green, monomer B in blue. Transparent outlines show the same cryo-EM maps at a lower contour level. **e**–**h**, Models of ADP- (**e**), ATP- (**f**), AMPPNP- (**g**) and ADP-Vi-bound MutS (**h**). Gray ribbons indicate approximate positions of the missing clamp and lever domains poorly defined in the cryo-EM map. Connector and mismatch domains of monomer B are colored pink and surrounded by a dashed black line. A central helix in the connector domain (residues 231–248) is colored orange, with N and C termini colored blue and red, respectively. **i**, Negative-stained 2D classes of ADP-bound MutS showing the flexibility of the MutS dimer. **j**, Transition of the ATPase domains from ADP_2- to **k**, ATP:ADP-bound MutS resulting from a 35° rotation of the two monomers. Yellow arrows indicate helix dipole attracted by the negative charge of triphosphate in the opposite monomer. **l**, Transition of ATPase domains from ATP:ADP- to $AMPPNP_2$-bound MutS. Gray coloring represents the original position of monomer B before 6° rotation, dashed red line represents the rotation axis of monomer B. **m**, Model of $AMPPNP_2$-bound MutS without movement of the mismatch and connector domains. Red star indicates the clash the between mismatch-binding domains of monomers A (green) and B (gray). Core domain and ATPase domain are omitted for clarity. **n**, Rotation of mismatch and connector domain circumvents the clash with monomer A. **o**, The domains of MutS represented by different colors and indicated by name.

a resolution of 4.8, 3.3, 3.4 and 3.7 Å, respectively (Fig. 1, Table 1 and Extended Data Figs. 1–4). All structures were obtained by incubation of 4 µM MutS with 3 mM nucleotide for 5 min at 4 °C in buffer containing Mg^{2+}, before plunge-freezing in liquid ethane. We observed that three of the four conditions produced a single conformational state: an open form for ADP_2 and a closed form for both $AMPPNP_2$ and ADP-Vi_2. In contrast, in the sample incubated with ATP we observed both the open ADP_2-bound form and the closed ATP:ADP-bound form, indicating that under these conditions MutS can hydrolyze ATP.

Table 1 | Cryo-EM data collection, refinement and validation statistics

	ADP (EMD-13073) (PDB 7OU2)	ATP:ADP (EMD-13074) (PDB 7OU4)	AMPPNP (EMD-13063) (PDB 7OT0)	ADP-Vi (EMD-13071) (PDB 7OU0)
Data collection and processing				
Magnification	130,000	105,000	130,000	130,000
Voltage (kV)	300	300	300	300
Electron exposure ($e^-/Å^2$)	57	54	54	34
Defocus range (μm)	1.0 to 2.5	0.5 to 2.0	1.0 to 2.5	−0.5 to 2.0
Pixel size (Å)	1.060	0.836	1.060	0.660
Symmetry imposed	C1	C1	C1	C1
Initial particle images (no.)	110,730	527,979	294,231	496,416
Final particle images (no.)	41,730	151,672	147,899	81,316
Map resolution (Å)	4.8	3.3	3.4	3.8
FSC threshold	1.43	1.43	1.43	1.43
Map resolution range (Å)	4.5 to >10.7	3.3 to >4.8	3.4 to >4.3	3.7 to >10.7
Refinement				
Initial model used (PDB code)	1E3M	AMPPNP	1E3M	AMPPNP
Model resolution (Å)	7.8	3.6	3.4	4.0
FSC threshold	0.5	0.5	0.5	0.5
Map sharpening *B* factor ($Å^2$)	−50	−80	−80	−70
Model composition				
Non-hydrogen atoms	10,338	10,955	10,336	10,800
Protein residues	1,320	1,393	1,318	1,373
B factors ($Å^2$)				
Protein	35-159	35-337	34-307	21-306
R.m.s. deviations				
Bond lengths (Å)	0.013	0.012	0.014	0.013
Bond angles (°)	1.552	1.492	1.783	1.627
Validation				
MolProbity score	1.20	1.31	1.16	1.26
Clashscore	4.19	5.73	3.71	4.94
Poor rotamers (%)	0.09	0.96	0	0.09
Ramachandran plot				
Favored (%)	98.46	98.39	98.46	97.34
Allowed (%)	1.46	1.61	1.46	2.36
Disallowed (%)	0.08	0	0.08	0

In all four structures the clamp domains are poorly resolved, suggesting that they are flexible in the absence of DNA. This flexibility is most pronounced in the structure of ADP-bound MutS, where the lever and clamp domains adopt different conformations that can be discerned by negative-stain EM (Fig. 1i). In contrast, in the presence of DNA, the clamp domains regain the rigidity needed to exert the force required to bend DNA during mismatch recognition[25,26], or to move DNA by 20 Å during transformation into the clamp state[22].

The four structures show increasing compaction from the open form in the ADP_2-bound state to the ATP:ADP-bound state, to the most compact $AMPPNP_2$- and ADP-Vi_2-bound states, which adopt identical conformations. A similar ATP (or AMPPNP)-dependent closing of MutS homologs has previously been observed by small-angle X-ray scattering[27,28], negative-stain EM[18] and Förster resonance energy transfer (FRET) studies[29,30]. In contrast, several X-ray crystallography structures of ATP- or AMPPNP-bound MutS do not show closing of the MutS dimer, possibly due to crystal packing that restricts movement[31,32]. In our cryo-EM structures, transition from ADP_2- to ATP:ADP-bound MutS is characterized by a 35° rotation of the two monomers towards each other around a pivot point located at the interface of the two ATPase domains (Fig. 1j,k and Supplementary Video 1). It is noteworthy that the addition of a single PO_4^{3-} ion (from ADP to ATP) results in a dramatic increase in resolution, from 4.8 to 3.3 Å, due to the more stable conformation adopted by MutS in the ATP-bound form. The subsequent transition from ATP:ADP to $AMPPNP_2$ (or ADP-Vi_2) is the result of an additional ~6° twist of the ATPase domains along the axis of a helix at the bottom of the ATPase domain that further closes nucleotide binding sites (Fig. 1l and Supplementary Videos 1 and 2). This rotation also brings the mismatch-binding domains closer, which would result in a clash of the two domains (Fig. 1m). However, in monomer B the mismatch-binding and connector domains have rotated ~160° downwards, thus avoiding a clash with monomer A (Fig. 1n and Supplementary Video 3). Interestingly, the same rotation of the mismatch-binding and connector domains is also observed in the DNA-bound clamp state, adopted by MutS following mismatch and

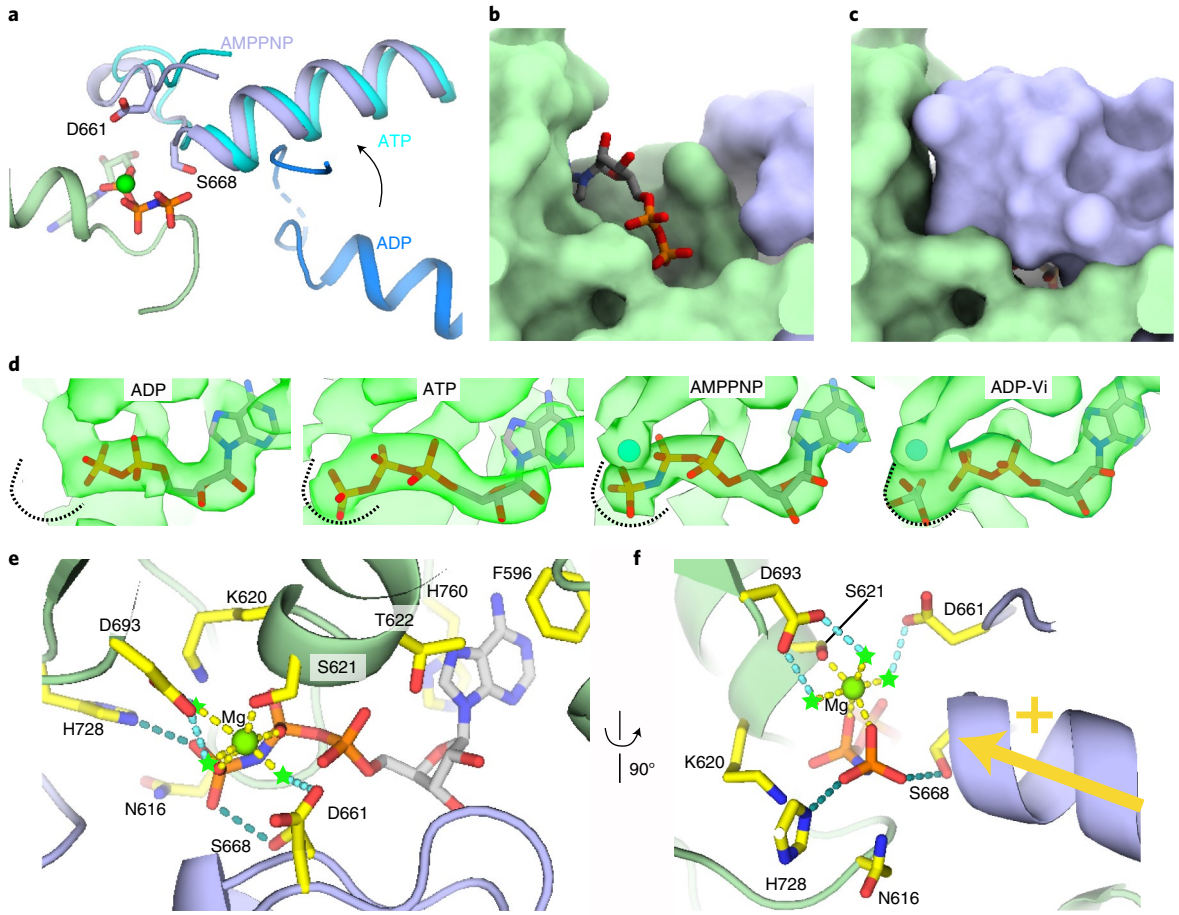

Fig. 2 | Closing of the MutS dimer completes the ATPase active site. a, Movement of the signature loop and helix of monomer B towards the nucleotide in monomer A. Monomer A is shown in green, with AMPPNP and residues Asp661 and Ser668 as sticks, and monomer B in dark blue (ADP-bound), light blue (ATP-bound) and pale blue (AMPPNP-bound). **b**,**c**, Surface representation of nucleotide binding site of ADP_2- (**b**) and ATP:ADP-bound MutS (**c**). Monomer A in green, monomer B in blue and ADP molecules shown as sticks. **d**, Close-up of cryo-EM maps for nucleotide binding sites in ADP_2-, ATP:ADP-, $AMPPNP_2$- and ADP-Vi_2-bound states. Dashed curved lines denote the boundary of the electron density map in the ADP-Vi_2-bound state. **e**, Close-up of the composite ATP binding site showing interactions with AMPPNP. Interacting residues are shown as yellow sticks and hydrogen bonds as dashed lines. Green stars denote the predicted position of water molecules. **f**, 90° Rotation of the view shown in **e**.

ATP binding[22,33]. However, in the clamp state both MutS monomers have rotated connector and mismatch domains due to the presence of DNA. In this state, DNA and the rotated domains of MutS form the binding site for MutL[22,33] that, together with MutS, initiates the repair cascade.

Finally, of the four structures, only the ADP-bound state is compatible with DNA binding because closing of the lever domains in the ATP:ADP- and $AMPPNP_2$/ADP-Vi_2-bound structures blocks the DNA entry channel. This suggests that both monomers need to have hydrolyzed ATP before MutS can bind DNA.

Closing of MutS completes ATPase active site formation. Like all ABC ATPases, the MutS ATPase domains are composite active sites where residues from both monomers are required for ATP hydrolysis[34]. The four current structures illustrate how the two ATPase domains of both monomers combine to complete the MutS active site during ATP hydrolysis (Fig. 2a). Completion of the ATPase active site is driven by the negative charge of the γ-phosphate in ATP that forms an attractive force to the positive charge of the helix dipole[35], and is deposited via a serine (Ser668 in MutS) in the opposing monomer[36] (Figs. 1j,k and 2f). In the open, ADP_2-bound form the nucleotide is exposed and free to exchange with ATP molecules from solution (Fig. 2b). In contrast, in the closed ATP:ADP- and $AMPPNP_2$/ADP-Vi_2-bound structures, the nucleotides in both monomers are encapsulated and probably slowed on leaving the active site (Fig. 2c).

In the ATP-bound site of the ATP:ADP structure, the signature motif (GxSTF, residues 666–670)[37] of the opposing monomer is further from the triphosphate tail as compared to the structure with AMPPNP and ADP-Vi (Fig. 2a). In addition, only weak density for Mg^{2+} is observed, indicative of low occupancy (Fig. 2d). In contrast, in the structures of $AMPPNP_2$/ADP-Vi_2-bound MutS the signature loop has moved closer to the phosphate tail of the nucleotide in the opposing monomer and aids in coordination of the magnesium ion that shows well-defined density (Fig. 2d–f). These two states of the nucleotide binding site (suboptimal conformation in the ATP:ADP state and optimal conformation in the $AMPPNP_2$ and ADP-Vi_2 states) may be the reason for the biphasic ATP hydrolysis rate observed in stopped-flow experiments on *E. coli* and *Thermus aquaticus* (Taq) MutS. In those cases, an initial burst of ATPase activity is followed by a slower steady-state activity[38,39]. It is possible that these two rates represent an initial double-ATP occupancy of nucleotide binding sites that are optimal for hydrolysis, followed by a slower rate that may be caused by asymmetric occupancy (ADP:ATP) that is less optimal for hydrolysis and dictated by the alternating ATPase domains[40].

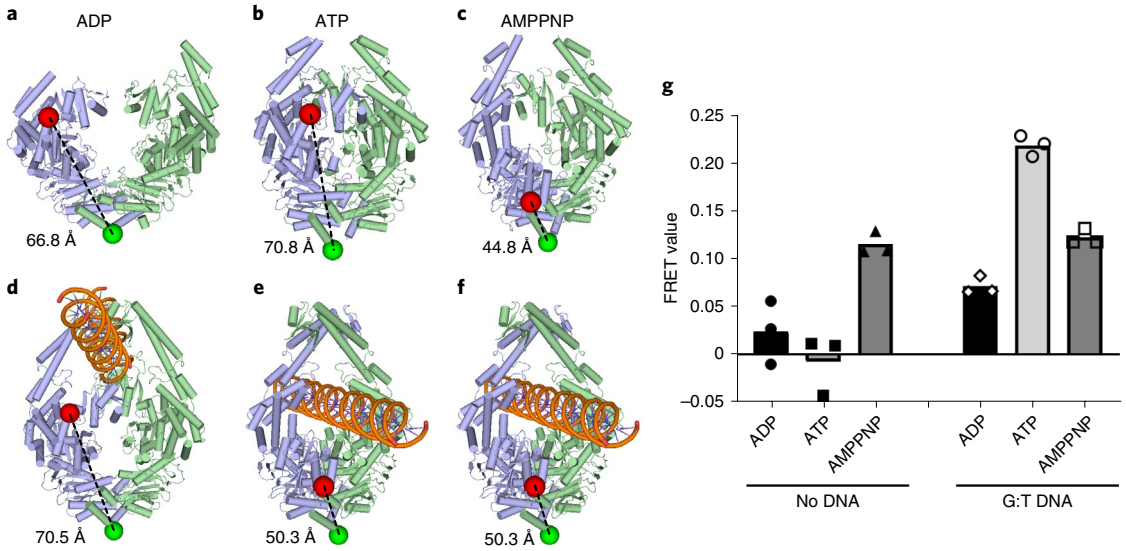

Fig. 3 | Two ATPs are needed for MutS clamp formation. a–c, Structures of ADP_2- (**a**), ATP:ADP- (**b**) and $AMPPNP_2$-bound MutS (**c**). Positions of residues 246 and 798 are denoted by red and green spheres, respectively. **d–f**, Structures of DNA-bound MutS in the presence of ADP (**d**)[25], ATP (**e**) and AMPPNP (**f**)[22]. **g**, Relative change in FRET values between fluorescently labeled residues 246 and 798 upon addition of different nucleotides and DNA. Higher FRET values indicate shorter distances.

The active site conformation of the $AMPPNP_2$ and ADP-Vi_2 structures is identical except for the position of the γ-phosphate that, in the ADP-Vi_2 structure, is replaced by the VO_4^{3-} ion which adopts a pentavalent coordination and has moved away from the β-phosphate, mimicking a post-hydrolysis transition state (Fig. 2d). Because $AMPPNP_2$/ADP-Vi_2 structures represent hydrolysis-competent forms, we now discuss the nucleotide binding site in more detail. The adenosine moiety of the nucleotide is held in place by Phe596 of monomer A (Phe596^A) and His760^A that stack on the base, while Asp616^A, Lys620^A and Thr622^A of the Walker A motif (P-loop, residues 614–622) bind the phosphate tail. Mg^{2+} is coordinated by oxygens of the β- and γ-phosphate of ATP^A and Ser621^A. The three water molecules that complete the octahedral coordination of Mg^{2+} observed in the crystal structure of MutS bound to a mismatch and ATP[31] are not defined in our cryo-EM maps, but are compatible with the position of Asp693^A and Asp661 from monomer B (Asp661^B; Fig. 2e,f). Asp661^B can complement the nucleotide binding site of monomer A due to closing of the MutS dimer, which also brings Ser668^B in close proximity to the γ-phosphate of ATP^A. Ser668 is part of the signature motif found in ABC ATPases (sequence GxSTF[37]) and is located immediately upstream of a helix with its N terminus pointed towards the nucleotide in the opposite monomer. This helix deposits the positive charge of its helix dipole onto the negatively charged phosphate tail of the nucleotide through Ser668^B (Fig. 2f). With the reduced charge on the phosphate tail and proper coordination of Mg^{2+}, an activated water molecule can perform a nucleophilic attack on the γ-phosphate. It has been proposed that, in the ABC ATPase Rad50, the equivalent of histidine 728^A can activate a water molecule to perform nucleophilic attack on the γ-phosphate[41]. This was corroborated by recent quantum mechanical and molecular mechanical modeling of the ABC transporter HlyB[42]. Accordingly, in our structure His728 is well positioned to activate a water molecule because it points towards the γ-phosphate of AMPPNP. Mutation of any of the residues in the ATP active site described above results in reduction or loss of ATPase activity (Supplementary Table 1).

Clamp-state MutS requires two ATP molecules. The structures of $AMPPNP_2$- and ADP-Vi_2-bound MutS show a large conformational change of the mismatch and connector domains in one of the monomers (Fig. 1n) that is identical to that observed in clamp-state MutS[22,43]. In the ATP:ADP-bound structure, however, this conformational change is absent, suggesting that a single ATP bound in the MutS dimer is insufficient to generate enough force to displace the mismatch and connector domains. This observation is consistent with a previous report showing that both monomers need to bind ATP to transform yeast MSH2-MHS6 into a DNA sliding clamp[44]. To determine whether this is indeed the case, we measured the FRET signal between two fluorophores located on the connector domain (residue 246) of one monomer and on the ATPase domain (residue 798) of the opposing monomer (Fig. 3). Rotation of the connector domain reduces the distance between these two residues and consequently increases energy transfer between the two fluorophores. In the presence of ADP, we observed a low FRET signal as predicted from the distance in the ADP-bound structure (Fig. 3). Similarly, in the presence of ATP there was no increase in FRET signal. In contrast, using the nonhydrolyzable analog AMPPNP we observed an increase in FRET signal as expected from the predicted rotation of the mismatch and connector domains observed in the AMPPNP-bound structure.

In the presence of mismatched DNA and ADP we observed an increase in FRET signal, possibly due to the reduced flexibility of MutS on DNA compared to apo MutS, which is highly flexible in the absence of DNA (Fig. 1i). In the presence of mismatched DNA and ATP we observed a strong increase in FRET signal brought about by the formation of clamp-state MutS, in which the mismatch and connector domains of both monomers had moved closer to the ATPase domains[22,33]. In the presence of DNA and AMPPNP we also observed an increase in FRET signal, although not as strong, possibly due to DNA-free MutS dimers that, in the presence of AMPPNP, are closed (Fig. 1g) and unable to bind DNA. This is in agreement with the observation that preincubation of MutS with AMPPNP reduces DNA binding[45–47].

Taken together our results indicate that, in the absence of DNA during steady-state hydrolysis, the MutS dimer binds only one ATP, consistent with the alternating ATPase domains of MutS observed in multiple species[41,48,49] and the slow, steady-state ATP hydrolysis rate[30]. Single ATP occupancy in the MutS dimer is not sufficient to induce conformational change. This was also observed in mismatch-bound MutS that can exist with a single nucleotide

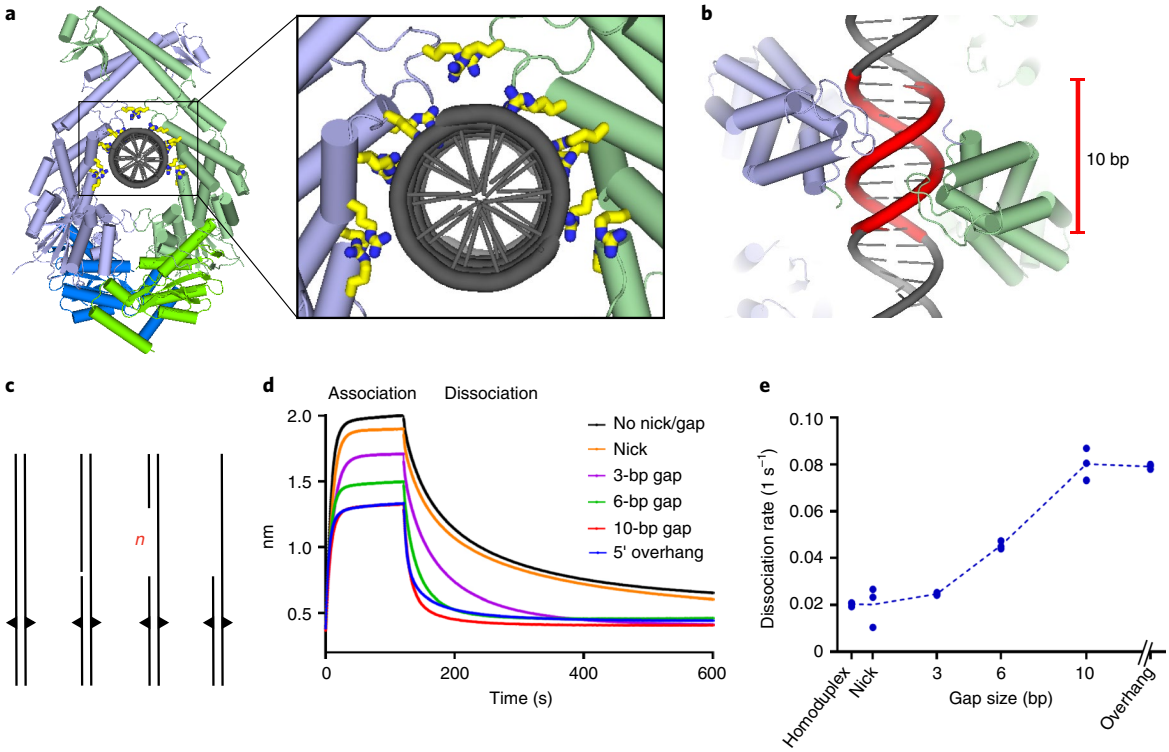

Fig. 4 | Release of MutS from DNA at a single-stranded gap. a, Close-up of the protein–DNA interaction in the clamp state of MutS[22]. Arginines and lysines that contact DNA are denoted by yellow sticks. **b**, Footprint of clamp-state MutS dimer on DNA covers 10 bp. **c**, Schematic representation of different DNA oligos used in the DNA release experiment; *n* represents the size of the gap, which is equal to three, six or ten bases. **d**, Association and dissociation of MutS on different DNA substrates with blocked ends (not shown) in the presence of 2 mM ATP as measured by BLI. **e**, Dissociation rates derived from binding curves shown in **d**. Dots denote rates calculated from three independent experiments.

triphosphate bound, but not with two[50]. Concurrently, in the cryo-EM structure of clamp-state MutS, both monomers contain nucleotide triphosphate in their nucleotide binding site[22]. Moreover, DNA binding may actually promote binding of the two ATP molecules that are needed to induce conformational change into the clamp state. The structures of MutS bound to homoduplex and mismatched DNA show the open conformation of the ATPase domains[22] that permits free exchange with ATP, giving MutS the potential to load two ATP molecules. This is consistent with the rapid release of ADP from mismatch-bound MutS, but not from free MutS[17,51].

dsDNA prevents nucleotide release from clamp-state MutS. Upon mismatch and ATP binding, MutS transforms into the sliding clamp that remains trapped on DNA but can freely slide on it until it reaches a stretch of ssDNA or a double-strand break where it can dissociate[18–21]. How MutS is able to remain in the clamp state on DNA for prolonged periods is not known. One possibility is that ATP cannot be hydrolyzed in the clamp state, thus keeping MutS in a closed state. However, comparison of the recent structure of clamp-state MutS on DNA[22] reveals that the position of ATPase domains is identical to that found in our ADP-Vi_2 structure, which mimics a post-hydrolysis transition state (Extended Data Fig. 4f). This implies that clamp-state MutS is capable of hydrolysis and that it is not ATP that keeps the dimer clamped around the DNA, in agreement with a recent observation that Taq MutS can hydrolyze ATP in the clamp state[52]. Rather, it appears that it is DNA that keeps the dimer closed. In the sliding clamp structure, the lever domains of the two monomers form an arc that surrounds the DNA duplex and interacts with the DNA backbone through multiple residues with a footprint of around ten base pairs (bp) (Fig. 4a,b). In this conformation, the ATPase domains are closed and nucleotides are trapped in the nucleotide binding sites (Fig. 2c). Correspondingly, clamp-state MutS can release DNA only at open ends or ssDNA[18–21]. Large stretches of ssDNA are produced during downstream events of the mismatch repair cascade through the action of a DNA helicase and DNA exonucleases, which are likely to be encountered by clamp-state MutS, in contrast to double-strand breaks, which are not known to be repaired by MMR. To measure the minimal length of the ssDNA gap needed to release clamp-state MutS, we used biolayer interferometry (BLI) to measure the release from a DNA substrate containing a mismatch and ssDNA gaps of different length in the presence of 2 mM ATP (Fig. 4c). The dissociation rate of MutS clamps increased with the size of the single-stranded gap, from 0.02 s^{-1} on dsDNA or nicked DNA until reaching a plateau at 0.08 s^{-1} at a gap of ten nucleotides or longer (Fig. 4d, e). This ten-nucleotide gap is equal in size to the DNA footprint of the MutS dimer (Fig. 4b), fitting with the notion that, as interactions with dsDNA are lost the dimer is no longer able to remain clamped around DNA and consequently falls off. Hence, by generating ssDNA gaps, UvrD and exonuclease not only remove the mismatch but also provide a simple release mechanism for MutS which would otherwise remain trapped on DNA.

Discussion

DNA and ATP coordinate sequential steps of the MMR cascade. It is well documented that mismatch and ATP binding by MutS are jointly required to initiate the repair cascade. Biochemical evidence has demonstrated that, after mismatch binding, MutS undergoes an ATP-dependent conformational change that transforms it into a sliding clamp that can dissociate only from open DNA ends[18,19] or ssDNA[20,21]. Importantly, only in this sliding clamp

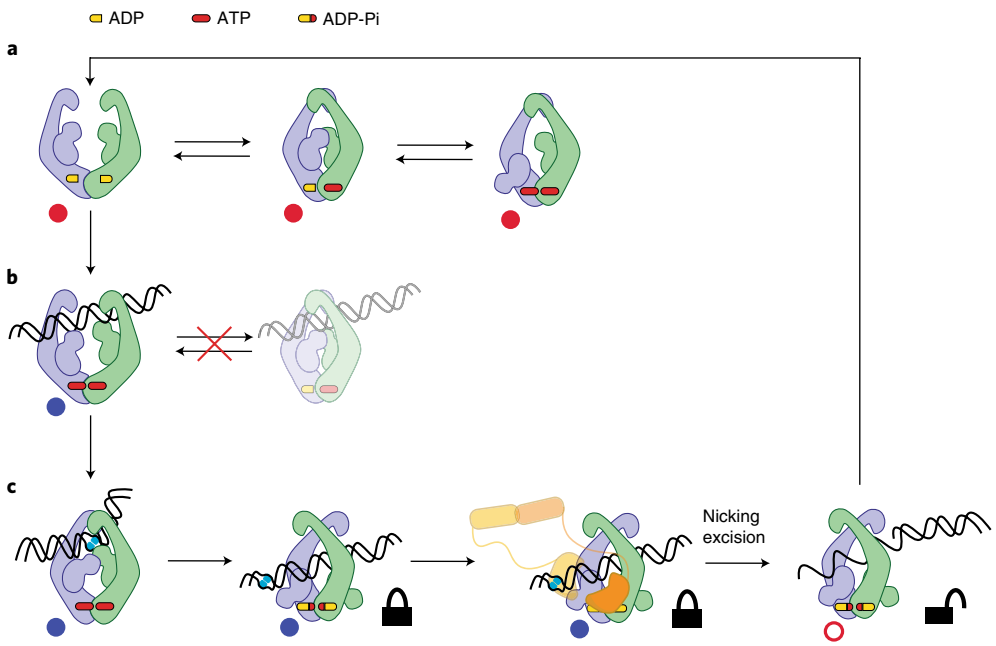

Fig. 5 | ATP and DNA combine to create sequential steps of the repair cascade. a–c, Cartoon representation of the different steps of the DNA mismatch repair cascade derived from current and recent cryo-EM work. Red dots indicate structures presented in this study, blue dots indicate cryo-EM and X-ray structures presented in previous work[22]. Red circle indicates predicted structure based on data presented in Fig. 4. **a**, In the absence of DNA, the two monomers can freely close and open upon ATP binding and hydrolysis. **b**, When bound to homoduplex DNA, the MutS dimer can no longer close and is therefore not able to hydrolyze ATP (right). The open form of MutS on DNA can freely exchange ADP for ATP. **c**, Upon mismatch binding, MutS transforms into a sliding clamp that can hydrolyze ATP but is locked by dsDNA. In this sliding clamp, conformation MutS can recruit MutL (orange) onto DNA and initiate the repair cascade. Only upon encountering ssDNA can MutS dissociate faster from DNA and return to the open, ADP-bound form that can rebind a new DNA substrate.

conformation is MutS able to recruit MutL and initiate repair[16,17]. More recently, single-molecule studies have revealed multiple states of MutS when transitioning from ADP to the ATP state[29,52,53]. Thus far, however, a detailed mechanistic and structural description of how DNA and ATP affect the conformational dynamics of MutS has not been available.

The four structures presented here provide a detailed view of the mechanism of ATP hydrolysis and show how opening and closing of the dimer is at the core of catalytic activity. Combined with our recent structures of DNA-bound MutS during different stages of the repair process[22], our new structures reveal how ATP hydrolysis and DNA binding cooperate to coordinate the sequential steps of the MMR pathway. In the absence of DNA, the two MutS monomers freely open and close during ATP binding and hydrolysis (Fig. 5a). Due to the alternating ATPase domains of MutS[40], only one ATP is bound by the dimer, preventing it from assuming the most compact form, which is reached only with either the non-hydrolyzable ATP analog AMPPNP or the transition-state analog ADP-Vi (Fig. 1g,h). When MutS associates with homoduplex DNA in search of a mismatch, DNA holds the dimer in an open form[22], thus preventing ATP hydrolysis (Fig. 5b). In this open conformation the two nucleotide binding sites are freely accessible, enabling loading of two ATP molecules. This open conformation of ATPase domains is retained when MutS first encounters a mismatch[25,26]. However, mismatch binding induces small rearrangement of the clamp domains that acts as a licensing step enabling MutS to transform into the sliding clamp[22], but not before both monomers bind ATP. This two-nucleotide requirement was also observed by mass spectrometry[50] and mutagenesis analysis of the yeast MSH2-MSH6 heterodimer[44].

Transformation into the clamp state involves rotation of ~160° of the mismatch and connector domains of both monomers and a ~20-Å translation of DNA towards the center of the dimer as the lever domains cross each other, firmly locking DNA in the MutS clamp (Fig. 5c)[22]. In the clamp state, although ATPase active sites are compatible with ATP hydrolysis (Extended Data Fig. 4f)[52], due to interactions between DNA and the MutS lever domains the two monomers cannot open, keeping MutS trapped on DNA. Importantly, only in this clamp state is MutS able to load MutL onto DNA, which in turn activates MutH to incise the mismatched strand[54]. Following this event, a large section of ssDNA is generated by the combined action of UvrD and 5′–3′ or 3′–5′ exonucleases[12,14]. These regions of ssDNA enable the release of MutS from DNA[20,21] and its resetting for a new round of mismatch binding.

As the repair process continues, the size of the ssDNA gap increases towards the mismatch, reducing the time that MutS molecules reside on DNA until the mismatch is removed and no further loading of MutS molecules takes place. Due to the low processivity of UvrD in the absence of MutS and MutL[13], DNA excision will cease shortly after the removal of a mismatch, leaving DNA open for resynthesis by a DNA polymerase[14] and thus completing the repair process.

Online content

Any methods, additional references, Nature Research reporting summaries, source data, extended data, supplementary information, acknowledgements, peer review information; details of author contributions and competing interests; and statements of data and code availability are available at https://doi.org/10.1038/s41594-021-00707-1.

Received: 2 June 2021; Accepted: 24 November 2021;
Published online: 10 January 2022

References

1. Li, Z., Pearlman, A. H. & Hsieh, P. DNA mismatch repair and the DNA damage response. *DNA Repair (Amst.)* **38**, 94–101 (2016).
2. Jiricny, J. Postreplicative mismatch repair. *Cold Spring Harb. Perspect. Biol.* **5**, a012633 (2013).
3. Welsh, K. M., Lu, A. L., Clark, S. & Modrich, P. Isolation and characterization of the *Escherichia coli* mutH gene product. *J. Biol. Chem.* **262**, 15624–15629 (1987).
4. Junop, M. S., Yang, W., Funchain, P., Clendenin, W. & Miller, J. H. In vitro and in vivo studies of MutS, MutL and MutH mutants: correlation of mismatch repair and DNA recombination. *DNA Repair (Amst.)* **2**, 387–405 (2003).
5. Hall, M. C. & Matson, S. W. The *Escherichia coli* MutL protein physically interacts with MutH and stimulates the MutH-associated endonuclease activity. *J. Biol. Chem.* **274**, 1306–1312 (1999).
6. Kadyrov, F. A., Dzantiev, L., Constantin, N. & Modrich, P. Endonucleolytic function of MutLα in human mismatch repair. *Cell* **126**, 297–308 (2006).
7. Fukui, K., Nishida, M., Nakagawa, N., Masui, R. & Kuramitsu, S. Bound nucleotide controls the endonuclease activity of mismatch repair enzyme MutL. *J. Biol. Chem.* **283**, 12136–12145 (2008).
8. Pluciennik, A. et al. PCNA function in the activation and strand direction of MutL endonuclease in mismatch repair. *Proc. Natl Acad. Sci. USA* **107**, 16066–16071 (2010).
9. Pillon, M. C., Miller, J. H. & Guarné, A. The endonuclease domain of MutL interacts with the β sliding clamp. *DNA Repair (Amst.)* **10**, 87–93 (2011).
10. Yang, H., Yung, M., Sikavi, C. & Miller, J. H. The role of *Bacillus anthracis* RecD2 helicase in DNA mismatch repair. *DNA Repair (Amst.)* **10**, 1121–1130 (2011).
11. Walsh, B. W. et al. RecD2 helicase limits replication fork stress in *Bacillus subtilis*. *J. Bacteriol.* **196**, 1359–1368 (2014).
12. Burdett, V., Baitinger, C., Viswanathan, M., Lovett, S. T. & Modrich, P. In vivo requirement for RecJ, ExoVII, ExoI, and ExoX in methyl-directed mismatch repair. *Proc. Natl Acad. Sci. USA* **98**, 6765–6770 (2001).
13. Yamaguchi, M., Dao, V. & Modrich, P. MutS and MutL activate DNA helicase II in a mismatch-dependent manner. *J. Biol. Chem.* **273**, 9197–9201 (1998).
14. Lahue, R. S., Au, K. G. & Modrich, P. DNA mismatch correction in a defined system. *Science* **245**, 160–164 (1989).
15. Goellner, E. M., Putnam, C. D. & Kolodner, R. D. Exonuclease 1-dependent and independent mismatch repair. *DNA Repair (Amst.)* **32**, 24–32 (2015).
16. Schofield, M. J., Nayak, S., Scott, T. H., Du, C. & Hsieh, P. Interaction of *Escherichia coli* MutS and MutL at a DNA Mismatch. *J. Biol. Chem.* **276**, 28291–28299 (2001).
17. Acharya, S., Foster, P. L., Brooks, P. & Fishel, R. The coordinated functions of the *E. coli* MutS and MutL proteins in mismatch repair. *Mol. Cell* **12**, 233–246 (2003).
18. Gradia, S. et al. hMSH2-hMSH6 forms a hydrolysis-independent sliding clamp on mismatched DNA. *Mol. Cell* **3**, 255–261 (1999).
19. Blackwell, L. J., Bjornson, K. P., Allen, D. J. & Modrich, P. Distinct MutS DNA-binding modes that are differentially modulated by ATP binding and hydrolysis. *J. Biol. Chem.* **276**, 34339–34347 (2001).
20. Heo, S. D., Cho, M., Ku, J. K. & Ban, C. Steady-state ATPase activity of *E. coli* MutS modulated by its dissociation from heteroduplex DNA. *Biochem. Biophys. Res. Commun.* **364**, 264–269 (2007).
21. Jeong, C. et al. MutS switches between two fundamentally distinct clamps during mismatch repair. *Nat. Struct. Mol. Biol.* **18**, 379–385 (2011).
22. Fernandez-Leiro, R. et al. The selection process of licensing a DNA mismatch for repair. *Nat. Struct. Mol. Biol.* **28**, 373–381 (2021).
23. Hingorani, M. M. Mismatch binding, ADP-ATP exchange and intramolecular signaling during mismatch repair. *DNA Repair (Amst.)* **38**, 24–31 (2016).
24. Davies, D. R. & Hol, W. G. J. The power of vanadate in crystallographic investigations of phosphoryl transfer enzymes. *FEBS Lett.* **577**, 315–321 (2004).
25. Lamers, M. H. et al. The crystal structure of DNA mismatch repair protein MutS binding to a G x T mismatch. *Nature* **407**, 711–717 (2000).
26. Obmolova, G., Ban, C., Hsieh, P. & Yang, W. Crystal structures of mismatch repair protein MutS and its complex with a substrate DNA. *Nature* **407**, 703–710 (2000).
27. Kato, R., Kataoka, M., Kamikubo, H. & Kuramitsu, S. Direct observation of three conformations of MutS protein regulated by adenine nucleotides. *J. Mol. Biol.* **309**, 227–238 (2001).
28. Hura, G. L. et al. Comprehensive macromolecular conformations mapped by quantitative SAXS analyses. *Nat. Methods* **10**, 453–454 (2013).
29. Qiu, R. et al. Large conformational changes in MutS during DNA scanning, mismatch recognition and repair signalling. *EMBO J.* https://doi.org/10.1038/emboj.2012.95 (2012).
30. Sharma, A., Doucette, C., Biro, F. N. & Hingorani, M. M. Slow conformational changes in MutS and DNA direct ordered transitions between mismatch search, recognition and signaling of DNA repair. *J. Mol. Biol.* **425**, 4192–4205 (2013).
31. Lamers, M. H. et al. ATP increases the affinity between MutS ATPase domains: Implications for ATP hydrolysis and conformational changes. *J. Biol. Chem.* **279**, 43879–43885 (2004).
32. Nirwal, S., Kulkarni, D. S., Sharma, A., Rao, D. N. & Nair, D. T. Mechanism of formation of a toroid around DNA by the mismatch sensor protein. *Nucleic Acids Res.* **46**, 256–266 (2018).
33. Groothuizen, F. S. et al. MutS/MutL crystal structure reveals that the MutS sliding clamp loads MutL onto DNA. *eLife* **4**, e06744 (2015).
34. Hopfner, K. P. Invited review: architectures and mechanisms of ATP binding cassette proteins. *Biopolymers* **105**, 492–504 (2016).
35. Hol, W. G. J. The role of the α-helix dipole in protein function and structure. *Prog. Biophys. Mol. Biol.* **45**, 149–195 (1985).
36. Hopfner, K. P. & Tainer, J. A. Rad50/SMC proteins and ABC transporters: unifying concepts from high-resolution structures. *Curr. Opin. Struct. Biol.* **13**, 249–255 (2003).
37. Acharya, S. Mutations in the signature motif in MutS affect ATP-induced clamp formation and mismatch repair. *Mol. Microbiol.* **69**, 1544–1559 (2008).
38. Bjornson, K. P., Allen, D. J. & Modrich, P. Modulation of MutS ATP hydrolysis by DNA cofactors. *Biochemistry* **39**, 3176–3183 (2000).
39. Antony, E. & Hingorani, M. M. Asymmetric ATP binding and hydrolysis activity of the *Thermus aquaticus* MutS dimer is key to modulation of its interactions with mismatched DNA. *Biochemistry* **43**, 13115–13128 (2004).
40. Lamers, M., Winterwerp, H. & Sixma, T. The alternating ATPase domains of the DNA mismatch repair enzyme MutS control DNA mismatch repair. *EMBO J.* **22**, 746–756 (2003).
41. Hopfner, K. P. et al. Structural biology of Rad50 ATPase: ATP-driven conformational control in DNA double-strand break repair and the ABC-ATPase superfamily. *Cell* **101**, 789–800 (2000).
42. Zhou, Y., Ojeda-May, P. & Pu, J. H-loop histidine catalyzes ATP hydrolysis in the *E. coli* ABC-transporter HlyB. *Phys. Chem. Chem. Phys.* **15**, 15811–15815 (2013).
43. Groothuizen, F. S. et al. Using stable MutS dimers and tetramers to quantitatively analyze DNA mismatch recognition and sliding clamp formation. *Nucleic Acids Res.* **41**, 8166–8181 (2013).
44. Mazur, D. J., Mendillo, M. L. & Kolodner, R. D. Inhibition of Msh6 ATPase activity by mispaired DNA induces a Msh2(ATP)-Msh6(ATP) state capable of hydrolysis-independent movement along DNA. *Mol. Cell* **22**, 39–49 (2006).
45. Galio, L., Bouquet, C. & Brooks, P. ATP hydrolysis-dependent formation of a dynamic ternary nucleoprotein complex with MutS and MutL. *Nucleic Acids Res.* **27**, 2325–2331 (1999).
46. Biswas, I. & Vijayvargia, R. Heteroduplex DNA and ATP induced conformational changes of a MutS mismatch repair protein from *Thermus aquaticus*. *Biochem. J.* **347**, 881–886 (2000).
47. Cristóvão, M. et al. Single-molecule multiparameter fluorescence spectroscopy reveals directional MutS binding to mismatched bases in DNA. *Nucleic Acids Res.* **40**, 5448–5464 (2012).
48. Iaccarino, I., Marra, G., Palombo, F. & Jiricny, J. hMSH2 and hMSH6 play distinct roles in mismatch binding and contribute differently to the ATPase activity of hMutSα. *EMBO J.* **17**, 2677–2686 (1998).
49. Studamire, B., Quach, T. & Alani, E. *Saccharomyces cerevisiae* Msh2p and Msh6p ATPase activities are both required during mismatch repair. *Mol. Cell. Biol.* **18**, 7590–7601 (1998).
50. Monti, M. C. et al. Native mass spectrometry provides direct evidence for DNA mismatch-induced regulation of asymmetric nucleotide binding in mismatch repair protein MutS. *Nucleic Acids Res.* **39**, 8052–8064 (2011).
51. Gradia, S., Acharya, S. & Fishel, R. The human mismatch recognition complex hMSH2-hMSH6 functions as a novel molecular switch. *Cell* **91**, 995–1005 (1997).
52. Hao, P. et al. Recurrent mismatch binding by MutS mobile clamps on DNA localizes repair complexes nearby. *Proc. Natl Acad. Sci. USA* **117**, 17775–17784 (2020).
53. LeBlanc, S. J. et al. Coordinated protein and DNA conformational changes govern mismatch repair initiation by MutS. *Nucleic Acids Res.* **46**, 10782–10795 (2018).
54. Au, K. G., Welsh, K. & Modrich, P. Initiation of methyl-directed mismatch repair. *J. Biol. Chem.* **267**, 12142–12148 (1992).

Methods

Materials. All chemicals were purchased from Sigma-Aldrich unless indicated otherwise. All chromatography columns were purchased from Cytiva.

Protein expression and purification. The dimeric version of *E. coli* MutS, R840E[43], was cloned into the vector pETNKI-his3C-LIC-amp[55]. Plasmids were transformed in *E. coli* BL21(DE3) pLysS cells and plated onto Luria–Bertani agar with 50 μg ml^{-1} chloramphenicol and 100 μg ml^{-1} ampicillin. All colonies were scraped from the plate and distributed over 6 × 500 ml of Terrific Broth supplemented with 50 μg ml^{-1} chloramphenicol, 100 μg ml^{-1} ampicillin, 1 mM $MgCl_2$ and 1% glucose. Cells were grown at 37 °C to optical density 600 ~7, diluted with one volume of Terrific Broth and induced with a final concentration of 1 mM isopropyl 1-thio-β-D-galactopyranoside for 2 h at 30 °C. Proteins were purified using a procedure modified from ref. [56]. All subsequent steps were performed using basic buffer (25 mM HEPES pH 7.5, 5 mM $MgCl_2$, 2 mM DTT) supplemented with NaCl or imidazole as indicated.

Harvested cells were resuspended in basic buffer with 500 mM NaCl and 10 mM imidazole and lysed by sonication, followed by centrifugation at 14,000*g*. The supernatant was injected onto a 5-ml HisTrap HP column and eluted with a gradient to 500 mM imidazole in basic buffer with 500 mM NaCl. Pooled fractions were diluted in ten volumes of basic buffer, injected onto a 5-ml HiTrap heparin column and eluted with a gradient to 1 M NaCl in basic buffer. Pooled fractions were concentrated and injected into a gel filtration column (Superdex 200 16/600) equilibrated in basic buffer with 100 mM NaCl. Pooled fractions were injected onto a 5-ml HiTrap Q column equilibrated in the same buffer and eluted with a gradient to 1 M NaCl in basic buffer.

Cryo-EM sample preparation and imaging. Purified MutS was diluted to 4 μM in 20 mM Tris pH 8.5, NaCl 150 mM, 5 mM $MgCl_2$, 2 mM DTT and 0.01% (w/v) Tween 20. Diluted protein was incubated with 3 mM of either ADP, ATP, AMPPNP or ADP-Vi. Cu R1.2/1.3 or R2/1 holey carbon grids (Quantifoil) were glow discharged at 25 mA for 45 s using the Emitech K950 apparatus (Quorum). Next, 3 μl of MutS nucleotide sample was adsorbed onto glow-discharged grid, blotted for 1 s at 80% humidity at 4 °C and flash-frozen in liquid ethane using an EM GP plunge freezer (Leica). All cryo-EM data were collected at the The Netherlands Center for Electron Nanoscopy (NeCEN).Grids were loaded into a Titan Krios (FEI) electron microscope operating at 300 kV with a K2 or K3 direct electron detector equipped with a Bioquantum energy filter (Gatan). The slit width of the energy filter was set to 20 eV. Images were recorded with EPU software (Thermo Fisher Scientific) in counting mode. Dose, magnification and effective pixel size are detailed in Table 1.

Cryo-EM image processing. All image processing was performed using Relion 3.1 (ref. [57]). Images were drift corrected using Relion's own (CPU-based) implementation of the UCSF Motioncor2 program[58], and defocus was estimated using gCTF[59]. Laplacian-of-Gaussian-based autopicking was performed on a subset of micrographs and picked particles were two-dimensionally (2D) classified. Selected classes from the 2D classification were used as references to autopick particles from the full datasets. After two or three rounds of 2D classification, classes with different orientation were selected for initial model generation in Relion. The initial model was used as reference for three-dimensional (3D) classification into different classes. The selected classes from 3D classification were then subjected to 3D autorefinement. Defocus values were further refined using CTF Refinement in Relion, followed by Bayesian polishing. Another round of 3D autorefinement was performed on these polished particles. The density for MutS ADP-Vi was improved by using focused classification without image alignment. All maps were postprocessed to correct for modulation transfer function of the detector and sharpened by applying a negative B factor, as determined automatically by Relion. A soft mask was applied during postprocessing to generate FSC curves to yield maps of average resolution 3.4 Å for MutS AMPPNP, 4.8 Å for MutS ADP, 3.8 Å for MutS ADP-Vi and 3.3 Å for MutS ATP.

Model building was performed using Coot[60], REFMAC5 (ref. [61]), the CCPEM suite[62] and Phenix[63]. For the ATP:ADP, $AMPPNP_2$ and $ADPVi_2$ structures we could build detailed models into the high-resolution maps, while for ADP_2 this was limited to rigid-body fitting of existing structures and restrained refinement with REFMAC. Details on model refinement and validation are given in Table 1. In brief, model building started by rigid-body fitting of known crystal structures (PDB 1E3M and PDB 5AKB) into the different maps using Pymol (Schrödinger) or Chimera[64]. Next, we carried out one round of refinement in Refmac5 using jelly-body restraints and the model was further adjusted in Coot. After initial refinement, we generated improved-resolution EM maps using the SuperEM method[65], which aided in model building and refinement. A final refinement round and validation of the model and data were carried out using Refmac5 with proSmart[66] restraints within the CCPEM suite, with additional model validation using MolProbity[67] within Phenix[63].

Negative-stain EM sample preparation and imaging. Purified MutS was diluted to 0.04 μM in 20 mM Tris pH 8.5, NaCl 150 mM, 5 mM $MgCl_2$, 2 mM DTT, 0.01% Tween 20 and 1 mM ADP. Grids were glow discharged for 60 s at 25 mA using an EMITECH K950 apparatus. Three microliters of sample was absorbed to glow-discharged, carbon-coated copper grids (C-Flat200-CU) and incubated for 30 s before partial blotting. The grids were sequentially stained with 3 μl of 2.3% uranyl acetate, incubated for 30 s and then blotted dry. Micrographs were collected on an FEI Tecnai Biotwin electron microscope equipped with a LaB6 filament operated at 120 kV and ×49,000 nominal magnification. The total dose was 20 e$^-$/Å^2, and defocus values ranged from −0.5 to −3.0 μm. Images were collected with a FEI Eagle 4 × 4 K CCD camera with final pixel size of 4.44 Å.

Negative-stain image processing. All image processing was performed using Relion 3.1 (ref. [57]). Contrast transfer function estimation was performed with CTFFIND4.1 (ref. [68]). A small set of particles was manually picked, 2D classified and used as references for the autopicking procedure; 7,845 particles were extracted from a total of 73 micrographs. The extraction procedure was performed without inversion of contrast. Extracted particles were subjected to reference-free 2D average without performing CTF correction.

BLI of DNA substrates. Six different DNA substrates of varying gap length were prepared for assay (Supplementary Table 2). The substrates were prepared as follows: monovalent streptavidin and a 5′ biotinylated primer were mixed in a 1:1 ratio at a nominal concentration of 20 μM and purified via analytical gel filtration using a Superdex 200 increase (3.2/30) column (Cytiva) equilibrated in Tris 10 mM pH 8.0, NaCl 50 mM and EDTA 1 mM. Fractions containing biotinylated primer were mixed with the 5′ biotinylated DNA template to create the final DNA substrate. Efficient annealing of primer and template was confirmed with 15% polyacrylamide 0.5 × Tris Borate EDTA gel. Annealed substrates were stored at −20 °C at a concentration of 5 μM.

BLI DNA assay. Association and dissociation kinetics between MutS and DNA were observed using Octet RED96 (Sartorius). All interaction studies were performed with streptavidin biosensors (Sartorius) conjugated to biotinylate DNA substrates. All experiments were performed in the following buffer: HEPES 25 mM pH 7.5, NaCl 150 mM, $MgCl_2$ 5 mM, DTT 2 mM, BSA 0.5 mg ml^{-1} and Tween 20 0.01% (v/v). DNA substrates were added in the loading step at 100 nM, until the threshold value of 0.36 nm was reached. The association step was performed with MutS 200 nM in the presence of 2 mM ATP. The dissociation step was performed in buffer with 2 mM ATP. Kinetic analysis was performed using the Octet Data Analysis software package v.7.1, and figure plots were generated with Prism v.2.5.

FRET assay. Förster resonance energy transfer between the labeled connector domain of one subunit and the ATPase domain of the other was measured using heterodimeric MutS dimers similar to those described previously[43]. For labeling, proteins were diluted to 40 μM in 150 μl of buffer (10 mM HEPES/KOH pH 8.0, 200 mM KCl and 1 mM EDTA) and labeled with a fivefold molar excess of either Alexa Fluor 488 maleimide or Alexa Fluor 647 maleimide (Invitrogen) for 2 h on ice in the dark according to the the manufacturer's instructions. Excess dye was removed using Zeba Spin Desalting columns (Thermo Fisher Scientific). The degree of labeling was determined from absorbance spectra recorded at 220–700 nm (nanodrop) according to the manufacturer's instructions, as described previously[43]. Heterodimers were allowed to form by mixing 10 μM MutS798C labeled with Alexa Fluor 488 and MutS246C labeled with Alexa Fluor 647, and incubation on ice for at least 1.5 h in the absence of nucleotides in buffer (25 mM HEPES/KOH pH 7.5, 5 mM $MgCl_2$, 150 mM KCl and 0.05% (v/v) Tween 20). Aliquots of the reaction were flash-frozen in liquid nitrogen and stored at −80 °C. A 30-bp DNA substrate with a central G:T mismatch was prepared by annealing the T-strand (5′ dig-AATTGCACCGAGCTTGATCCTCGATGATCC-dig 3′) with the G-strand (5′ GGATCATCGAGGATCGAGCTCGGTGCAATT 3′; underlining denotes the G:T mismatch). The T-strand contains digoxigenin on either side, so that both DNA ends were blocked with 200 nM anti-digoxigenin Fab fragments (Roche Diagnostics)

MutS heterodimers (50 nM monomer) were preincubated in 200 μl of FB150 buffer (25 mM HEPES/KOH pH 7.5, 5 mM $MgCl_2$, 150 mM KCl, and 0.05 % (v/v) Tween 20) in 96-well plates at room temperature for 120 s. Next, 50 nM G:T DNA substrate was added followed by the addition of 1 mM ATP, ADP or AMPPNP (Jena Bioscience) and AMPPNP (Sigma-Aldrich).

FRET was determined by measuring fluorescence signals on a microplate reader (TECAN infinite F200, Tecan), both before and 10 min after the addition of the deoxynucleotide triphosphates. Fluorescence signals were measured in three channels (donor, acceptor, FRET) with the following filter combinations: donor excitation 450 nm (width 20 nm); emission 535 nm (width 25 nm); acceptor excitation 620 nm (width 10 nm); and emission 670 nm (width 25 nm); FRET excitation 485 nm (width 20 mm); emission 670 nm (width 25 nm) filter. Figure graphs were generated with Prism v.2.5.

Reporting Summary. Further information on research design is available in the Nature Research Reporting Summary linked to this article.

Data availability

Cryo-EM maps and atomic models have been deposited in the Electron Microscopy Database and Protein Data Bank, respectively, under accession code

nos. EMD-13073, PDB 7OU2, EMD-13074, PDB 7OU4, EMD-13063, PDB 7OTO, EMD-13071 and PDB 7OU0. Source data for the graphs in Figs. 3 and 4 are available with the paper online. Other requests should be addressed to Meindert Lamers (m.h.lamers@lumc.nl). Source data are provided with this paper.

References

55. Luna-Vargas, M. P. A. et al. Enabling high-throughput ligation-independent cloning and protein expression for the family of ubiquitin specific proteases. *J. Struct. Biol.* **175**, 113–119 (2011).
56. Feng, G. & Winkler, M. E. Single-step purifications of His6-MutH, His6-MutL and His6-MutS repair proteins of escherichia coli K-12. *Biotechniques* **19**, 956–965 (1995).
57. Zivanov, J. et al. New tools for automated high-resolution cryo-EM structure determination in RELION-3. *eLife* **7**, e42166 (2018).
58. Zheng, S. Q. et al. MotionCor2: anisotropic correction of beam-induced motion for improved cryo-electron microscopy. *Nat. Methods* **14**, 331–332 (2017).
59. Zhang, K. gCTF: real-time CTF determination and correction. *J. Struct. Biol.* **193**, 1–12 (2016).
60. Emsley, P., Lohkamp, B., Scott, W. G. & Cowtan, K. Features and development of Coot. *Acta Crystallogr. D Biol. Crystallogr.* **66**, 486–501 (2010).
61. Murshudov, G. N. et al. REFMAC5 for the refinement of macromolecular crystal structures. *Acta Crystallogr. D Biol. Crystallogr.* **67**, 355–367 (2011).
62. Nicholls, R. A., Tykac, M., Kovalevskiy, O. & Murshudov, G. N. Current approaches for the fitting and refinement of atomic models into cryo-em maps using CCP-EM. *Acta Crystallogr. D Struct. Biol.* **74**, 492–505 (2018).
63. Liebschner, D. et al. Macromolecular structure determination using X-rays, neutrons and electrons: recent developments in Phenix. *Acta Crystallogr. D Struct. Biol.* **75**, 861–877 (2019).
64. Pettersen, E. F. et al. UCSF Chimera – a visualization system for exploratory research and analysis. *J. Comput. Chem.* **25**, 1605–1612 (2004).
65. Venkata Subramaniya, S. R. M., Terashi, G. & Kihara, D. Super resolution Cryo-EM maps with 3D deep generative networks. Preprint at *bioRxiv* https://doi.org/10.1101/2021.01.12.426430 (2021).
66. Nicholls, R. A., Fischer, M., Mcnicholas, S. & Murshudov, G. N. Conformation-independent structural comparison of macromolecules with ProSMART. *Acta Crystallogr. D Biol. Crystallogr.* **70**, 2487–2499 (2014).
67. Williams, C. J. et al. MolProbity: more and better reference data for improved all-atom structure validation. *Protein Sci.* **27**, 293–315 (2018).
68. Rohou, A. & Grigorieff, N. CTFFIND4: fast and accurate defocus estimation from electron micrographs. *J. Struct. Biol.* **192**, 216–221 (2015).

Acknowledgements

We thank the staff of the LUMC EM facility and NeCEN for help with data collection and data processing. We thank R. Fernandez-Leiro for advice on data processing. This work was supported by a LUMC Research Fellowship to M.H.L., and a European Community's Horizon2020 Innovative Training Network Grant (no. 722433) to M.H.L. and P.F. Access to NeCEN was supported by Netherlands Electron Microscopy Infrastructure (project no. 184.034.014) of the National Roadmap for Large-Scale Research Infrastructure of the Dutch Research Council.

Author contributions

M.H.L. and A.B. conceived the overall experimental design. A.B. prepared samples and collected and processed cryo-EM data. A.B. purified proteins and performed BLI experiments. P.F. and V.K. designed and analyzed FRET experiments. V.K. performed FRET experiments, which were supervised by P.F. A.B. and M.H.L. wrote the manuscript with contributions from all authors.

Competing interests

The authors declare no competing interests.

Additional information

Extended data is available for this paper at https://doi.org/10.1038/s41594-021-00707-1.

Supplementary information The online version contains supplementary material available at https://doi.org/10.1038/s41594-021-00707-1.

Correspondence and requests for materials should be addressed to Meindert H. Lamers.

Peer review information *Nature Structural and Molecular Biology* thanks Jean-Baptiste Charbonnier and Keith Weninger for their contribution to the peer review of this work. Carolina Perdigoto and Beth Moorefield were the primary editors on this article and managed its editorial process and peer review in collaboration with the rest of the editorial team. Peer reviewer reports are available.

Reprints and permissions information is available at www.nature.com/reprints.

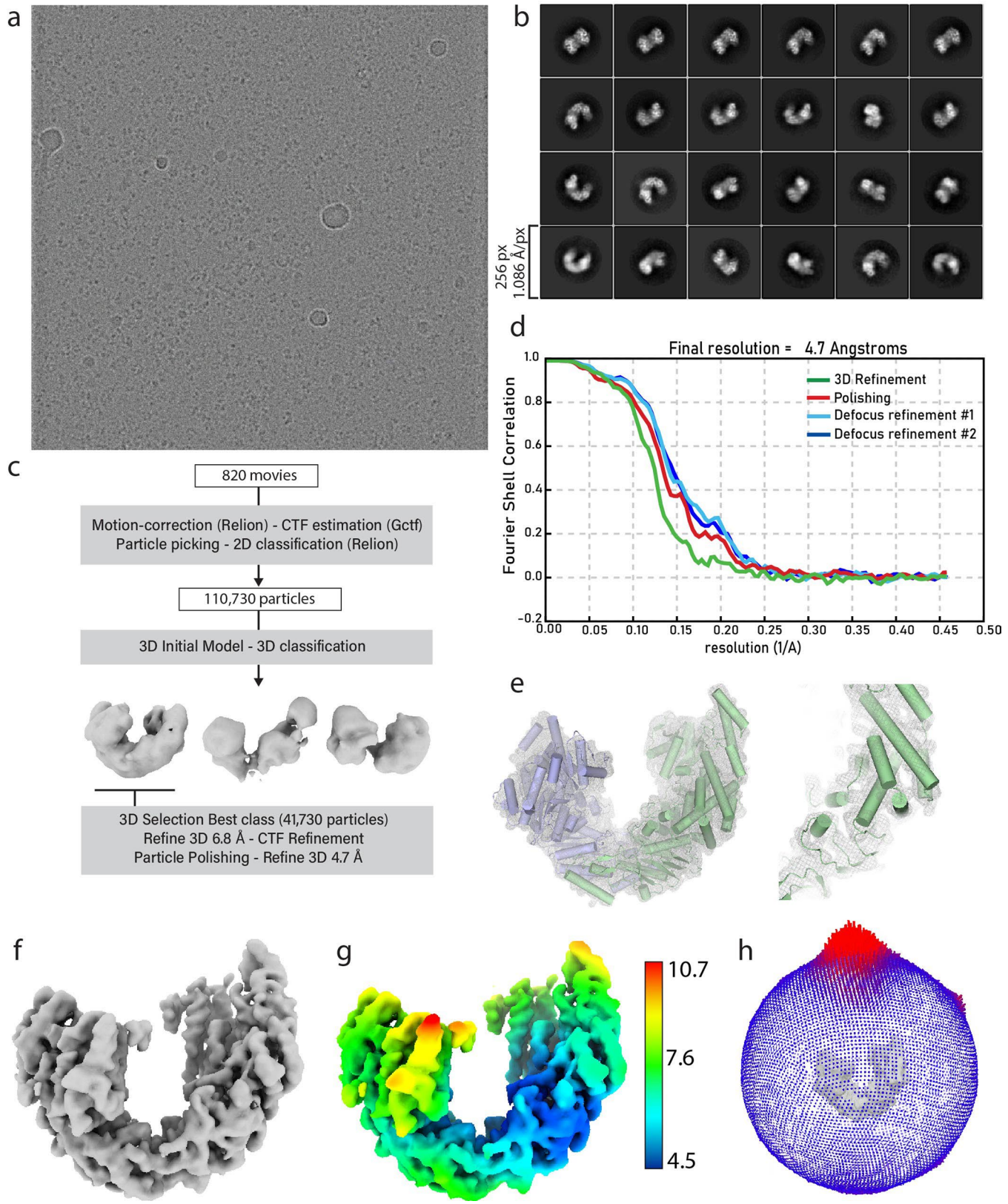

Extended Data Fig. 1 | CryoEM data analysis of ADP bound MutS. a, Representative micrograph. **b**, 2D class averages from full dataset. **c**, Schematic representation of main data processing procedures. See methods section for more details. **d**, Fourier Shell Correlation between half-maps from subsequent refinements in the processing procedures. **e**, Detail of model fit to map. **f**, Final map obtained applying SuperEM code to Relion post-processed map. **g**, final map colored by local resolution. **h**, Orientation distribution in final set of refined particles.

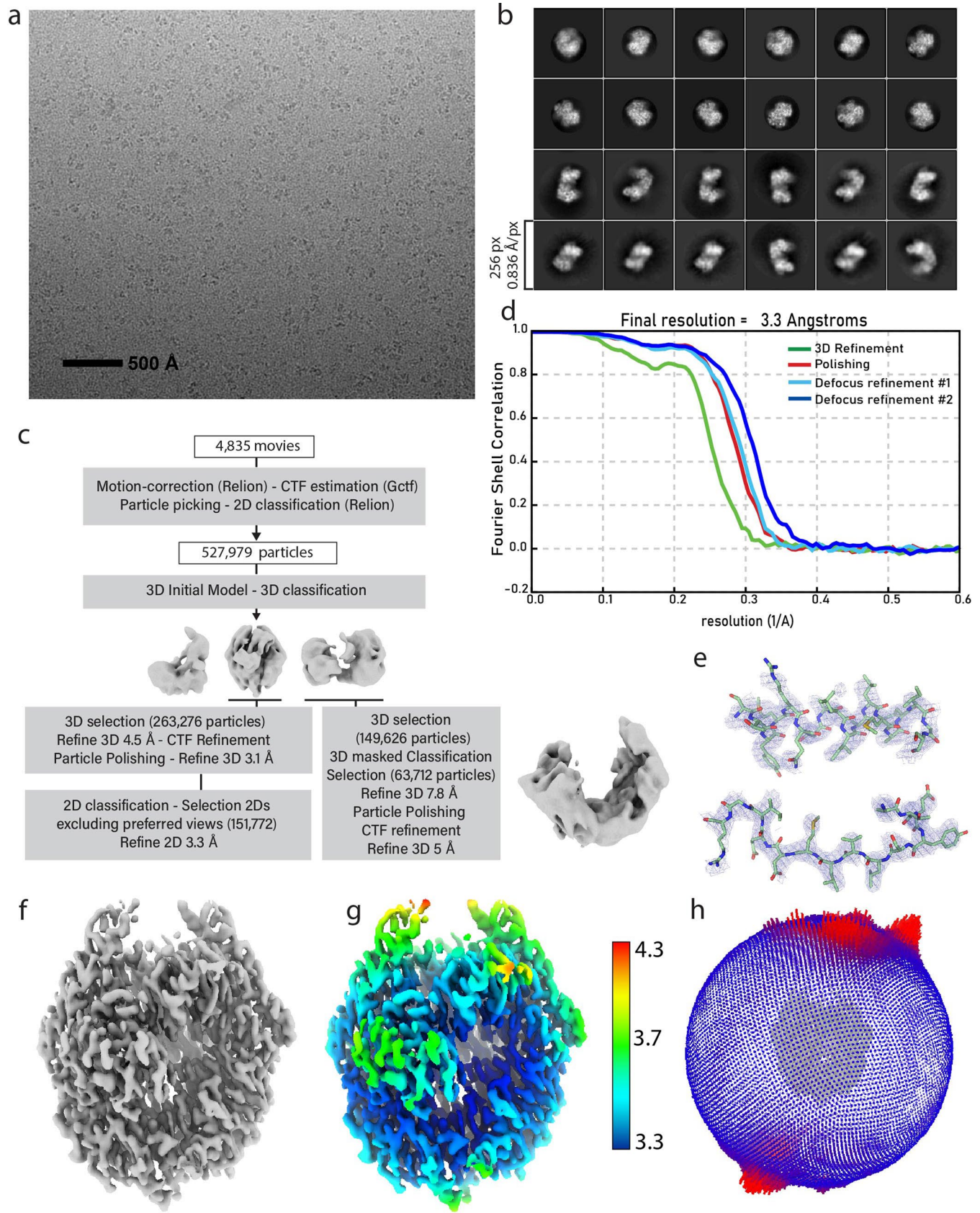

Extended Data Fig. 2 | CryoEM data analysis of ADP-ATP bound MutS. a, Representative micrograph. **b**, 2D class averages from full dataset. **c**, Schematic representation of main data processing procedures. See methods section for more details. **d**, Fourier Shell Correlation between half-maps from subsequent refinements in the processing procedures. **e**, Detail of model fit to map. **f**, Final map obtained applying SuperEM code to Relion post-processed map. **g**, final map colored by local resolution. **h**, Orientation distribution in final set of refined particles.

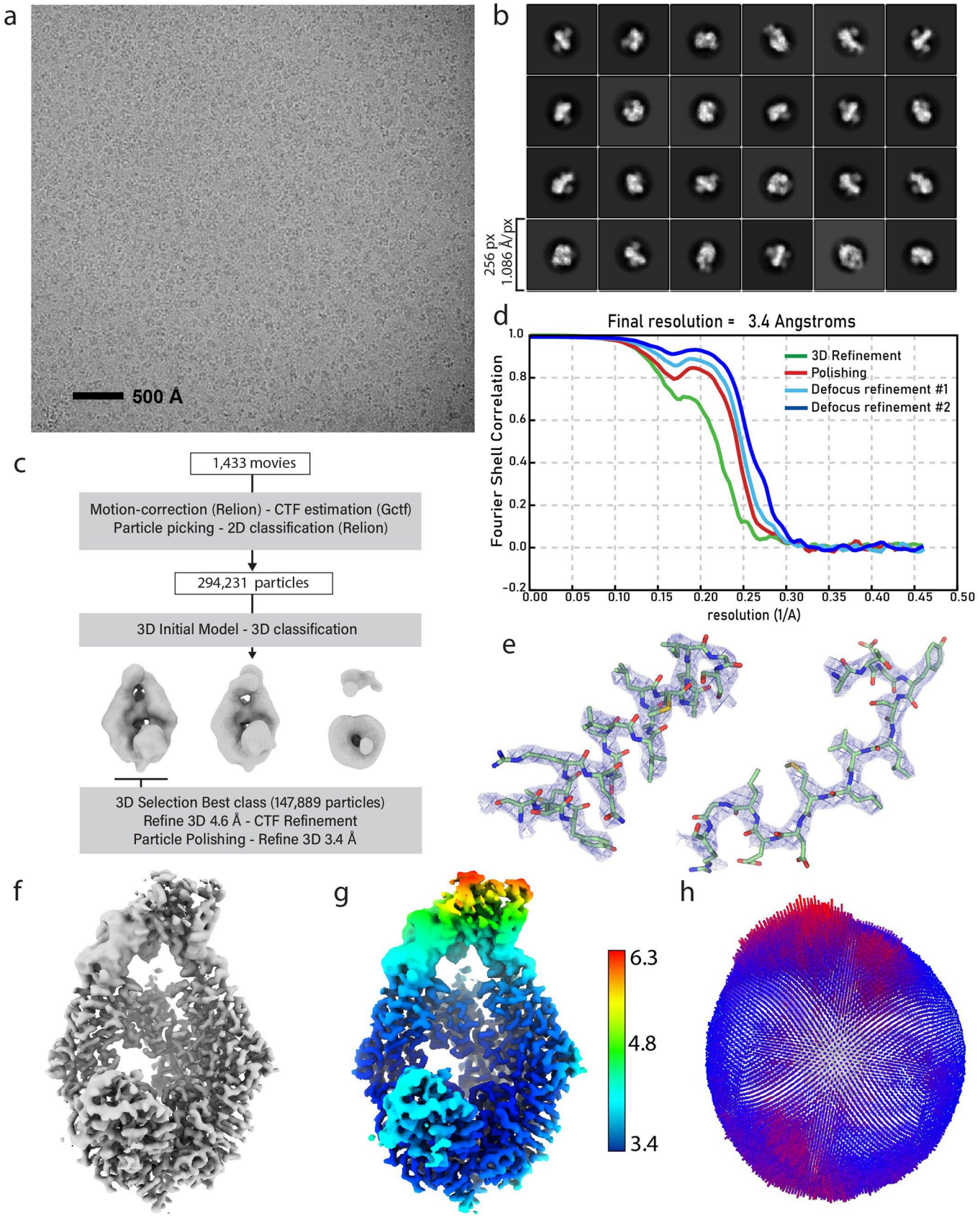

Extended Data Fig. 3 | CryoEM data analysis of ANPPNP bound MutS. a, Representative micrograph. **b**, 2D class averages from full dataset. **c**, Schematic representation of main data processing procedures. See methods section for more details. **d**, Fourier Shell Correlation between half-maps from subsequent refinements in the processing procedures. **e**, Detail of model fit to map. **f**, Final map obtained applying SuperEM code to Relion post-processed map. **g**, final map colored by local resolution. **h**, Orientation distribution in final set of refined particles.

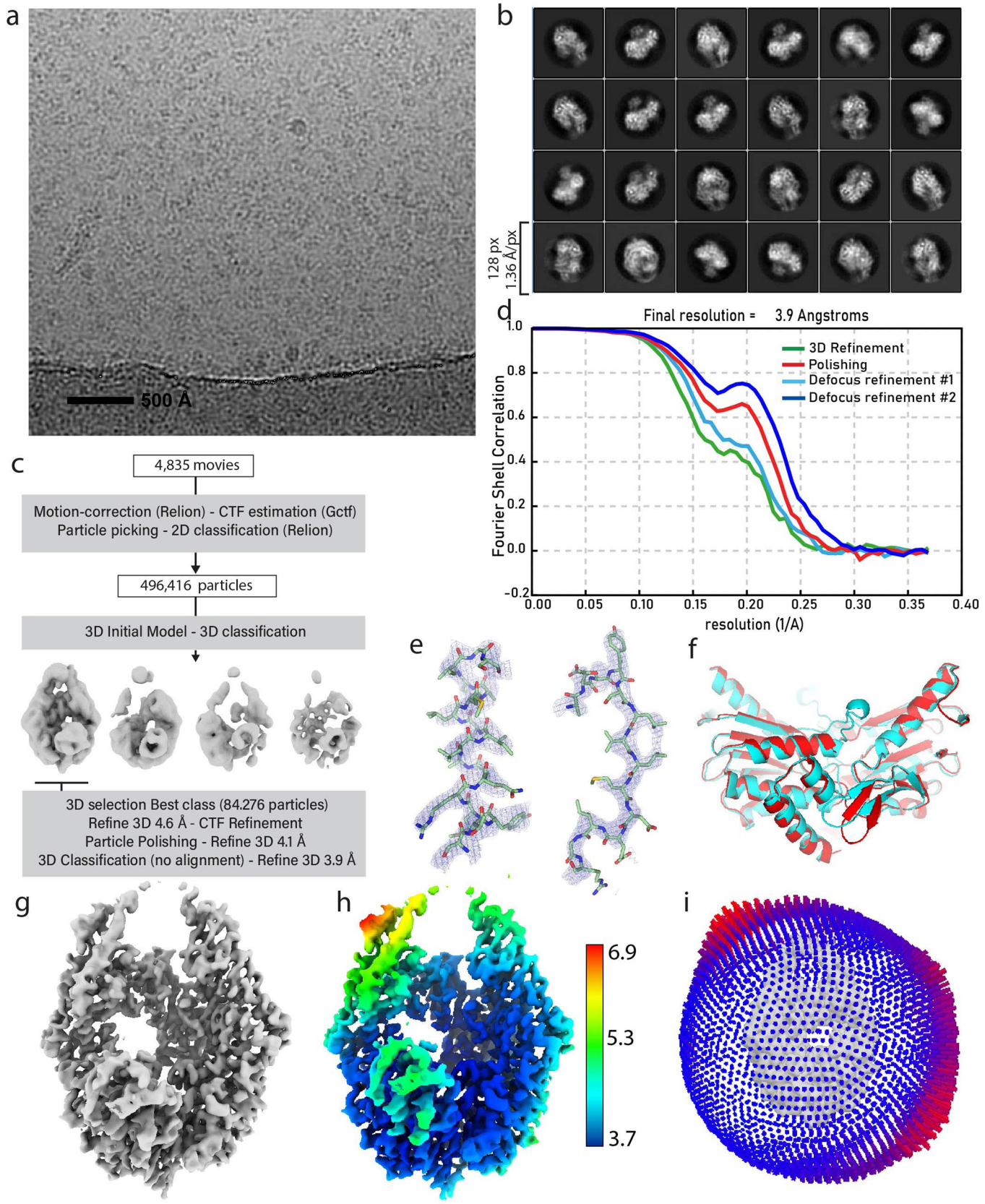

Extended Data Fig. 4 | CryoEM data analysis of ADP-Vi bound MutS. a, Representative micrograph. **b**, 2D class averages from full dataset. **c**, Schematic representation of main data processing procedures. See methods section for more details. **d**, Fourier Shell Correlation between half-maps from subsequent refinements in the processing procedures. **e**, Detail of model fit to map. **f**, Superimposition of nucleotide binding domains of MutS in ADP-Vi conformation and MutS in sliding clamp MutL bound conformation (Fernandez-Leiro 2021). **g**, Final map obtained applying SuperEM code to Relion post-processed map. **h**, final map colored by local resolution. **i**, Orientation distribution in final set of refined particles.

nature portfolio

Corresponding author(s): Meindert H. Lamers

Last updated by author(s): Nov 3, 2021

Reporting Summary

Nature Portfolio wishes to improve the reproducibility of the work that we publish. This form provides structure for consistency and transparency in reporting. For further information on Nature Portfolio policies, see our Editorial Policies and the Editorial Policy Checklist.

Statistics

For all statistical analyses, confirm that the following items are present in the figure legend, table legend, main text, or Methods section.

n/a	Confirmed
☐	☒ The exact sample size (*n*) for each experimental group/condition, given as a discrete number and unit of measurement
☐	☒ A statement on whether measurements were taken from distinct samples or whether the same sample was measured repeatedly
☒	☐ The statistical test(s) used AND whether they are one- or two-sided *Only common tests should be described solely by name; describe more complex techniques in the Methods section.*
☒	☐ A description of all covariates tested
☒	☐ A description of any assumptions or corrections, such as tests of normality and adjustment for multiple comparisons
☒	☐ A full description of the statistical parameters including central tendency (e.g. means) or other basic estimates (e.g. regression coefficient) AND variation (e.g. standard deviation) or associated estimates of uncertainty (e.g. confidence intervals)
☒	☐ For null hypothesis testing, the test statistic (e.g. *F*, *t*, *r*) with confidence intervals, effect sizes, degrees of freedom and *P* value noted *Give P values as exact values whenever suitable.*
☒	☐ For Bayesian analysis, information on the choice of priors and Markov chain Monte Carlo settings
☒	☐ For hierarchical and complex designs, identification of the appropriate level for tests and full reporting of outcomes
☒	☐ Estimates of effect sizes (e.g. Cohen's *d*, Pearson's *r*), indicating how they were calculated

Our web collection on statistics for biologists contains articles on many of the points above.

Software and code

Policy information about availability of computer code

Data collection	Cryo-EM: EPU (Software for Single Particle Analysis, Thermo Fisher Bio Layer Interferometry: Octet Data Acquisition 7.1 (Forte Bio)
Data analysis	Relion 3.1 Motioncorr2 v.1.2.1 Gctf v.1.06 CTFFIND v.4.1 Coot v 0.9.4 Phenix v.1.18.2 Octet Data Analysis 7.1 (Forte Bio) ccp-em v.1.5.0 (REFMAC5, MolProbity, Prosmart) Pymol v.2.5 Chimera v.1.13.1 ChimeraX

For manuscripts utilizing custom algorithms or software that are central to the research but not yet described in published literature, software must be made available to editors and reviewers. We strongly encourage code deposition in a community repository (e.g. GitHub). See the Nature Portfolio guidelines for submitting code & software for further information.

Data

Policy information about availability of data

All manuscripts must include a data availability statement. This statement should provide the following information, where applicable:

- Accession codes, unique identifiers, or web links for publicly available datasets
- A description of any restrictions on data availability
- For clinical datasets or third party data, please ensure that the statement adheres to our policy

Cryo-EM maps and atomic models have been deposited in the Electron Microscopy Database and Protein Data Bank, respectively, under accession codes EMD-13073, PDB 7OU2, EMD-13074, PDB 7OU4, EMD-13063, PDB 7OTO, EMD-13071 and PDB 7OU0. Other requests should be addressed to Meindert Lamers (m.h.lamers@lumc.nl).

Field-specific reporting

Please select the one below that is the best fit for your research. If you are not sure, read the appropriate sections before making your selection.

☒ Life sciences ☐ Behavioural & social sciences ☐ Ecological, evolutionary & environmental sciences

For a reference copy of the document with all sections, see nature.com/documents/nr-reporting-summary-flat.pdf

Life sciences study design

All studies must disclose on these points even when the disclosure is negative.

Sample size	No experiments were performed that were affected by sample size. Replicates were used instead.
Data exclusions	During Cryo-EM data processing 2D classes and 3D classes that did not posses high resolution features were removed following a standard procedure for Cryo-EM high resolution structure determination.
Replication	Bio Layer Interferometry and FRET experiments were all performed three times independently form one another. All replicates were successful.
Randomization	No experiments were performed that required randomization as the experiments outcomes are not influenced by researcher's bias.
Blinding	No experiments were performed that required blinding. Replicates of the experiments showed reproducible results.

Reporting for specific materials, systems and methods

We require information from authors about some types of materials, experimental systems and methods used in many studies. Here, indicate whether each material, system or method listed is relevant to your study. If you are not sure if a list item applies to your research, read the appropriate section before selecting a response.

Materials & experimental systems

n/a	Involved in the study
☒	☐ Antibodies
☒	☐ Eukaryotic cell lines
☒	☐ Palaeontology and archaeology
☒	☐ Animals and other organisms
☒	☐ Human research participants
☒	☐ Clinical data
☒	☐ Dual use research of concern

Methods

n/a	Involved in the study
☒	☐ ChIP-seq
☒	☐ Flow cytometry
☒	☐ MRI-based neuroimaging